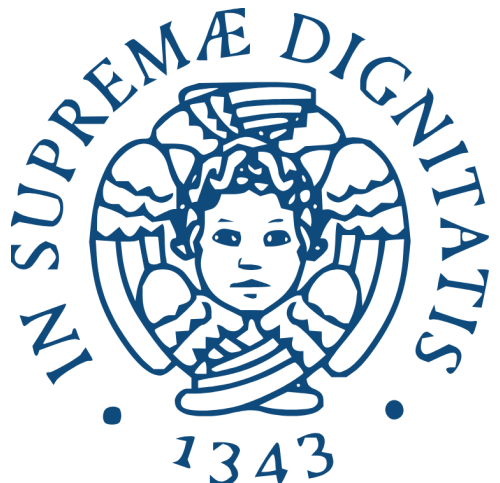


University of Pisa



Laboratory Report

# Analysis of the Periodic Emission from PSR J2229+6114 in the $\gamma$ -Ray Regime Using the Fermi Large Area Telescope (LAT)

## Professors:

Prof. Massimiliano Razzano  
Prof. Angelo Ricciardone  
Prof. Barbara Patricelli  
Prof. Andrea Pallottini

## Candidates:

Nicolò Aimone Braida (701844)  
Matilde Biscaro (702943)  
Lorenzo Nepi (701845)

## Abstract

Pulsars are highly magnetized, rapidly rotating neutron stars that emit periodic electromagnetic signals across a broad frequency range. The aim of this study is to investigate the periodic  $\gamma$ -ray emission from J2229+6114, a young radio pulsar located in the pulsar wind nebula (PWN) G106.65+2.96. The analyzed data were acquired by the Fermi Large Area Telescope (LAT) between 2008-10-05 and 2009-01-03. After a preprocessing phase, the data were analyzed to search for periodicity using the  $Z_n^2$  statistic. This yielded best-fit values of  $f_0 = 19.36391685 \pm 0.00000013$  Hz and a frequency derivative of  $f_1 = -(2.91921 \pm 0.00002) \times 10^{-12}$  Hz/s as the rotational parameters of the pulsar. Phaseograms were then constructed and analyzed in different energy ranges, highlighting the significant contribution of diffuse background emission. Finally, the main physical parameters characterizing the pulsar were calculated, yielding a rotation period  $P = 51.6424444386 \pm 0.000000004$  ms, a characteristic age  $\tau_c = 10515.7634 \pm 0.0002$  yr, a rotational energy loss rate  $\dot{E} = (2.23186924 \pm 0.0000003) \times 10^{37}$  erg/s, and a surface magnetic field strength  $B = (2.02916828 \pm 0.0000002) \times 10^{12}$  G. These results are coherent with values reported in the literature[1]. Finally, J2229+6114 was placed on the  $P - \dot{P}$  diagram, confirming its expected position using data from the ATNF Pulsar Catalogue [2]. Throughout the analysis, the need for a more detailed study of the data was emphasized, including the use of more accurate background and diffuse emission models, as well as improved uncertainty estimates based on statistical methods or a careful characterization of the instrument response.

## Contents

<b>1</b>	<b>Introduction</b>	1
<b>2</b>	<b>Theoretical Background</b>	2
2.1	Structure of Pulsars	2
2.2	Oblique Rotator Model	2
2.3	Pulsar evolution: $P - \dot{P}$ diagram	3
2.4	Periodicity test	3
<b>3</b>	<b>Fermi Gamma-ray Space Telescope</b>	3
3.1	Detector structure	4
3.2	Detector Methodology	4
3.3	Event Classification	5
<b>4</b>	<b>Data analysis</b>	5
4.1	Photon barycentering	6
4.2	Periodicity Search	6
4.3	Phaseogram Characterization	7
4.4	Physical Characterization of J2229+6114	7
4.5	J2229+6114 in the $P - \dot{P}$ diagram	7
<b>5</b>	<b>Discussion</b>	7
5.1	High Background Level	7
5.2	Phaseograms analysis	9
5.3	Physical quantities of J2229+6114	9
<b>6</b>	<b>Conclusion</b>	9
<b>References</b>		10

## 1 Introduction

Pulsars are highly magnetized, rapidly rotating neutron stars that emit periodic electromagnetic signals across a broad frequency range (mainly radio, X-ray, and  $\gamma$ -ray). The term *pulsar* (*pulsating radio source*) was first used to describe a class of radio sources discovered causally in England in 1967 by Jocelyn Bell and Antony Hewish, during a systematic survey of interplanetary scintillation of compact radio sources. Pulsars are characterized by the emission of short pulses that last only a few hundredths of a second and repeat at extraordinarily regular intervals, typically of the order of one second, with a timing precision of about one part in  $10^{10}$ . Although the total energy emitted by a pulsar is extremely high, the signal received on Earth is very weak, requiring highly sensitive instruments for detection.

Today, more than a thousand pulsars have been discovered. Their names are identified by the prefix PSR, followed by numerical identifiers corresponding to their celestial coordinates in right ascension (hours and minutes) and declination (degrees). Their galactic distribution follows the disk pattern, with a strong concentration along the galactic plane and toward the galactic center. Distance measurements have shown that most pulsars lie within a few kiloparsecs of the Sun, as those located farther away are too faint to be detected. This selection effect implies that the currently known population represents only a small fraction of the total pulsar population in our Galaxy.

In this experience, we analyze the  $\gamma$ -ray emission of PSR J2229+6114, a young radio pulsar located at  $(l, b) = (106^\circ.6, 2^\circ.9)$ . It powers the “Boomerang” arc-shaped pulsar wind nebula (PWN) G106.65+2.96, which is part of

the supernova remnant (SNR) G106.3+2.7 [10]. After a brief theoretical overview and a description of the instrument used (the Fermi Gamma-ray Space Telescope, formerly GLAST), we will extract the relevant observational data for J2229+6114 from the Fermi LAT archive, applying the required barycentering corrections to the photon arrival times. These preliminary steps will be performed using the dedicated tools provided by the Fermi LAT collaboration. Next, we will search for periodicity in the signal using the  $Z_n^2$  statistic. Based on the best-fit values found for the frequency and its derivative, we will then construct and analyze the resulting *phaseograms* and finally compute the physical parameters of J2229+6114 of interest in this study.

## 2 Theoretical Background

### 2.1 Structure of Pulsars

Pulsars are rapidly rotating neutron stars with extremely strong magnetic fields that emit pulsed radiation at highly regular intervals, typically on the order of one second. According to current theoretical models, neutron stars are structured as follows (see Fig.1):

- Outer crust: composed of ions and electrons, with a thickness of approximately 0.1 km and a density of  $4 \cdot 10^{11} \text{ g/cm}^3$ ;
- Inner crust: composed of ionic lattices immersed in a neutron superfluid, with a thickness of about 0.5 km and a density of  $2 \cdot 10^{14} \text{ g/cm}^3$ ;
- Outer liquid core: consisting of electrons ( $e^-$ ), muons ( $\mu^-$ ), neutron superfluid, and superconducting protons, with a thickness of roughly 10 km and a density approximately twice that of nuclear matter;
- Inner core: of unknown composition and structure, with an estimated density of about  $10^{15} \text{ g/cm}^3$ .

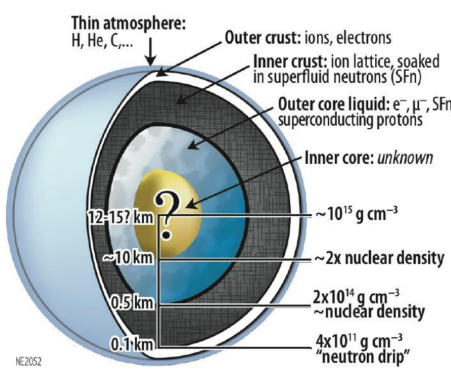


**Figure 1:** Structure of a neutron star according to current theoretical models.

### 2.2 Oblique Rotator Model

The model commonly used to explain the observed emissions from pulsars is the *oblique rotator model*, which assumes that the rotating neutron star possesses a magnetic dipole field whose axis is inclined by an angle  $\alpha$  with respect to the rotation axis. This model is based on several assumptions: the observer is located at a large distance

from the source, the pulsar is isolated and does not interact with other objects, and the current rotation period  $P$  is much longer than the initial period  $P_0$ .

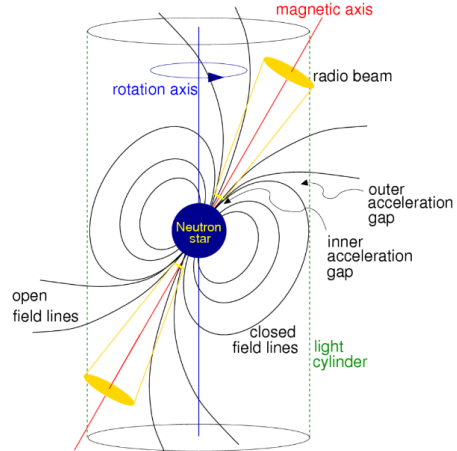


**Figure 2:** Dipole model.

Let  $m$  denote the magnetic dipole moment of the neutron star and  $\omega$  its angular velocity. The star emits an electromagnetic signal at the rotation frequency  $\nu = \omega/2\pi$ , typically a few Hz, with a radiated power described by the Larmor formula:

$$P_{\text{rad}} = \frac{2}{3} \frac{\dot{m}_\perp^2}{c^3}, \quad (1)$$

where  $m_\perp$  is the component of the magnetic dipole moment perpendicular to the line of sight. The energy is radiated at the expense of the rotational kinetic energy, given by:

$$E_{\text{rot}} = \frac{1}{2} I \omega^2 = \frac{2\pi^2 I}{P^2}, \quad (2)$$

where  $P$  is the rotation period (which is easier to measure than  $\omega$ ) and  $I$  is the moment of inertia of the star. Taking the time derivative of the rotational energy yields:

$$\dot{P}_{\text{rad}} = -\frac{dE_{\text{rot}}}{dt} = -I\omega\dot{\omega} = \frac{4\pi^2 I \dot{P}}{P^3}. \quad (3)$$

Eq. 3 can be rewritten by expressing the surface magnetic field strength  $B$  of the star, using the relation  $m_\perp = BR^3 \sin \alpha$  in Eq. 1, where  $R$  is the stellar radius. This leads to the expression:

$$B = \left( \frac{3c^3 I}{8\pi^2 R^6} \right)^{1/2} (P\dot{P})^{1/2}. \quad (4)$$

Substituting typical values for a neutron star, based on stellar physics (for example  $M_{\text{Ch}} \approx 1.44 M_\odot$ ,  $R \approx 10 \text{ km}$ , and  $I \approx 10^{45} \text{ g cm}^2$ ), we obtain:

$$\frac{B}{\text{Gauss}} \approx 3.2 \times 10^{19} \left( \frac{P\dot{P}}{\text{s}} \right)^{1/2}. \quad (5)$$

Finally, we define another fundamental quantity for describing pulsars: the *characteristic age*  $\tau_c$ . This parameter estimates the neutron star's age based on its rotational period and deceleration. Observationally speaking, the pulsar period increases systematically over time. Assuming that pulsars are born with a very short initial period ( $P_0 \ll P$ ) and that  $\dot{P}$  is constant, the pulsar's age can be estimated as:

$$\tau_c = \frac{P}{2\dot{P}}. \quad (6)$$

According to the model, as the pulsar rotates, it generates an electromotive force arising from the electric field induced by the motion of charged particles, which are subsequently accelerated along the magnetic field lines. Close to the star, electrons are expected to move at relativistic speeds, producing what is known as curvature radiation. Radio photons are primarily emitted from the polar regions, close to the neutron star's surface. In these zones, the magnetic fields are extremely intense, and high-energy photons can interact with the field, producing electron-positron pairs ( $e^+e^-$ ). This process leads to a suppression of the photon energy distribution at high energies.  $\gamma$ -ray photons, on the other hand, originate in the outer regions of the magnetosphere, farther from the pulsar surface, where the magnetic field strength is lower (*outer gap*, see Fig. 2). In these regions, pair production is less efficient, allowing gamma-ray photons to escape.

### 2.3 Pulsar evolution: $P-\dot{P}$ diagram

A  $P-\dot{P}$  diagram is a plot of a pulsar's rotation period  $P$  versus its time derivative  $\dot{P}$ , which reflects the rate at which the pulsar is slowing down. This diagram is a fundamental tool for the study and classification of pulsars, as it reveals key physical properties and evolutionary tracks. An example of  $P-\dot{P}$  is reported in Sec. 4.5. Using the equations presented in Sec. 2.2, it is possible to plot on this diagram the characteristic physical quantities of a pulsar, such as the magnetic field  $B$ , the rate of loss of rotational energy  $\dot{E}_{\text{rot}}$ , and the characteristic age  $\tau_c$ .

A pulsar is born as the remnant of a supernova explosion, appearing in the upper-left region of the diagram (where the iso-lines correspond to low  $\tau_c$  values). As it ages and spins down due to energy losses, it moves across the diagram with an approximately constant magnetic field strength  $B$ , following a trajectory toward the lower-right region. This evolution continues until it approaches the so-called *death line*, beyond which the pulsar is no longer able to sustain coherent radio emission. At this stage, pulsars enter what is commonly referred to as the *pulsar graveyard*. However, in some binary systems, a pulsar can "reborn" through mass accretion from its companion star. The pulsar gains angular momentum from the accreted matter, undergoing a spin-up process that significantly increases its rotation rate, leading to very short periods and thus very high frequencies. At the same time, its magnetic field tends to decay, resulting in a weaker surface field.

### 2.4 Periodicity test

The search for astronomical pulsed signals within noisy data is performed through Fourier analysis to search for periodicities, folding<sup>1</sup> in time series and statistic tests to establish how much the pulse profile departs from a null hypothesis where the periodic signal is absent.

The arrival times of each photon measured by the instrument can be reduced to a phase value in the interval

<sup>1</sup>Folding is a technique used to reveal periodicity in a time series. It consists of "folding" the observational data with respect to a trial period, mapping each event to its corresponding phase within that period. If the chosen period is correct, periodic signals add up coherently, enhancing the signal-to-noise ratio and allowing the detection of weak pulsed profiles.

0 to 1 by Taylor expansion

$$\phi_j(t) = \text{fractional part of } \{\phi(t_0) + f_0(t_0)(t_j - t_0) + 1/2 f_1(t_0)(t_j - t_0)^2 + \dots\}, \quad (7)$$

where  $t_0$  is the time epoch,  $f_0$  is the candidate pulse frequency and  $f_1 = \dot{f}_0$  is its time derivative.  $\phi(t_0)$  is the pulse phase at  $t_0$ , which is usually set to zero for unknown or candidate pulsars. In this experience, we will restrict our analysis to second-order terms.

Fourier analysis provides a set of candidate pulsations, among which the most promising astrophysical signal is selected using statistical indicators. In the X-ray and  $\gamma$ -ray regimes, sensitive statistical tests have been developed to detect signals whose pulsed components can be described as the sum of a relatively small number of sinusoidal harmonics. One of the most commonly used statistic test to detect signals for which the frequency and its derivative are known and can be used as initial parameters is the  $Z_n^2$  statistic, defined as [4]

$$Z_n^2 = \frac{2}{N} \sum_{k=1}^n \left[ \left( \sum_{j=1}^N \cos k\phi_j \right)^2 + \left( \sum_{j=1}^N \sin k\phi_j \right)^2 \right], \quad (8)$$

where  $N$  is the number of photons and  $n$  the number of harmonics considered. This formula evaluates how well the distribution of pulse phases is described by a series of  $n$  sinusoidal harmonics of increasing order.  $Z_n^2$  has a probability density function (p.d.f.) equal to that of  $\chi_{2n}^2$  (which has  $2n$  degrees of freedom). Given a certain number of trial pulse periods, one can calculate  $Z_n^2$  and select the periods that give the highest value for the statistic has the best candidates.

Other statistic tests are the  $\chi^2$  statistic and the H-test, which is employed to determine if the signal is described by a sum of harmonics and what is the best number of harmonics to describe the signal at the same time [3].

## 3 Fermi Gamma-ray Space Telescope

Launched in 2008, NASA's Fermi Gamma-ray Space Telescope (GLAST, see Fig. 3) is a space observatory designed to study the high-energy universe, particularly in the  $\gamma$ -ray regime. It is composed by two principal instruments:

- the Large Area Telescope (LAT), which can observe about a fifth of the sky at a time ( $\sim 20^\circ$ ), providing a wide field of view (FoV). It is able to scan the whole sky in two orbits ( $\sim 3$  hrs). The LAT detects gamma rays with energies ranging from 20 MeV to 300 GeV. The characteristics of the LAT are reported in Tab. 1;
- the Gamma-ray Burst Monitor (GBM). It is designed to observe gamma-ray bursts, which are sudden, brief flashes of gamma rays that occur about once a day at random positions in the sky. The GBM has such a large field-of-view that can see bursts from over two-thirds of the sky at once, providing locations for follow-up observations. The GBM is composed of two sets of detectors: 12 sodium iodide (NaI) scintillators and two cylindrical bismuth germanate (BGO) detectors. When gamma rays interact with these crystalline detectors, they produce flashes of visible light, that is used by the

**Table 1:** LAT Characteristics. [11]

Parameter	Value or Range
Energy Range	$\sim 20$ MeV to $>300$ GeV
Energy Resolution	$<15\%$ at energies $>100$ MeV
Effective Area	$>8,000 \text{ cm}^2$ maximum effective area at normal incidence
Single Photon Angular Resolution	$<0.15^\circ$ , on-axis, 68% containment radius for $E > 10$ GeV; $\sim 0.6^\circ$ , on axis, 68% containment radius for 1 GeV; $<3.5^\circ$ , on-axis, 68% containment radius for $E = 100$ MeV
Field of View	2.4 sr
Source Location Determination	$<0.5$ arcmin for high-latitude source
Point Source Sensitivity	$< 6 \times 10^{-9} \text{ ph cm}^{-2} \text{ s}^{-1}$ for $E > 100$ MeV, $5\sigma$ detection after 1 year sky survey
Time Accuracy	<10 microseconds, relative to spacecraft time
Background Rejection (after analysis)	<10% residual contamination of a high latitude diffuse sample for $E = 100$ MeV – 300 GeV
Dead Time	<100 microseconds per event

detector to locate the gamma-ray burst on the sky. The GBM works at a lower energy range than the LAT, so together they provide the widest range of energy detection in the gamma-ray regime for any satellite ever built.

During this experience, data from the LAT will be analyzed.



**Figure 3:** The Fermi spacecraft being readied for launch. The GBM detectors are labeled. [Image credit: Jim Grossmann, NASA, [11]].

### 3.1 Detector structure

The LAT consists of an array of 16 tracker (TKR) modules, 16 calorimeter (CAL) modules, and a segmented anti-coincidence detector (ACD). The TKR and CAL modules are mounted onto the central structure of the instrument. The structure of the LAT is reported in Fig. 4.

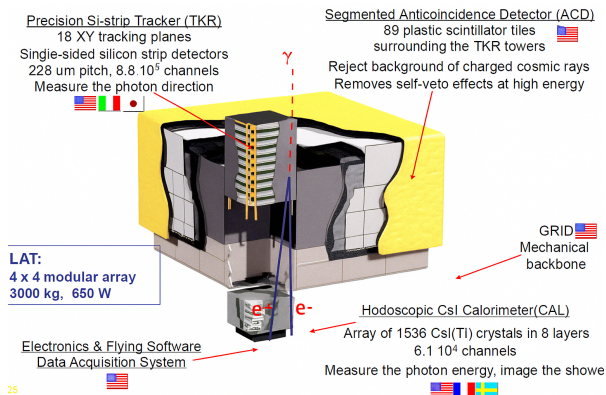


**Figure 4:** Structure of the LAT [11].

The core element of each tracker is the silicon strip detector (SSD), which is capable of recording the passage

of charged particles through the ionization of silicon, producing electron-hole pairs. Each SSD is 56  $\mu\text{m}$  wide, with a pitch of 288  $\mu\text{m}$ . A row of SSDs constitutes a ladder, whereas two ladders mounted one above the other and separated by a tungsten foil (used to convert incoming photons into electron-positron pairs) form a tray. Each tray enables a 2D reconstruction of the photon trajectory. Eighteen trays are vertically stacked to form a tower, providing full 3D reconstruction capabilities. The LAT is composed of 16 identical towers arranged in a  $4 \times 4$  grid. This configuration was specifically chosen to ensure redundancy, allowing the LAT to continue operating effectively even if some channels stop working. At the base of each tracker module is collocated a hodoscopic calorimeter, composed of 1536 CsI(Tl) crystal bars, organized into 8 layers.

Finally, the LAT is surrounded by a segmented ACD, consisting of 89 plastic scintillator tiles. The ACD fully encloses the tracker and is designed to reject charged cosmic-ray background while minimizing the rejection of photon-induced *backsplash* effects (see Sec. 3.2).

### 3.2 Detector Methodology

The LAT detects gamma rays by using a technique known as pair-conversion. When a gamma ray collides with a layer of tungsten ( $Z=74$ ) in the detector, it creates an electron and positron pair. These particles in turn hit another, deeper layer of tungsten, each creating further particles and so on. The direction of the incoming gamma ray is determined by tracking the direction of these cascading particles back to their source using high-precision silicon strip detectors. Furthermore, a separate detector (CAL) counts up the total energy of all the particles created. Since the total energy of the created particles depends on the energy of the original gamma ray, counting up the total energy allows to determine the energy of that  $\gamma$ -ray. In this way, Fermi is able to make  $\gamma$ -ray images of astronomical objects, while also determining the energy for each detected gamma ray. The schematic representation of the LAT detector is reported in Fig. 5.

Charged cosmic-ray particles incident on the LAT, which outnumber  $\gamma$ -ray photons by a factor ranging from  $10^2$  to  $10^5$ , also produce tracks within the LAT, generating a background of events that could potentially overwhelm the signal. To reject such background events, the LAT is surrounded by an Anti-Coincidence Detector (ACD), which detect these events and generate a veto signal.

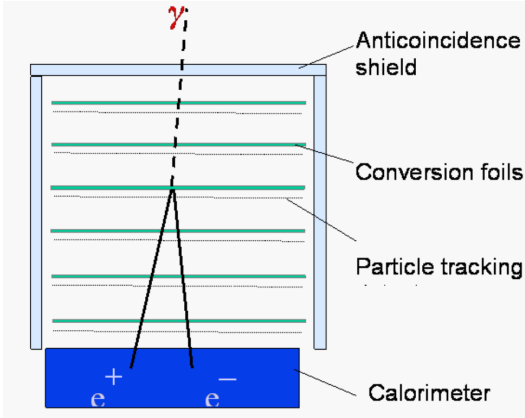


**Figure 5:** Schematic Structure of the LAT [11].

However, in some cases, secondary charged particles arising from the electromagnetic shower initiated by a high-energy photon in the calorimeter (potentially a valid event) can propagate upward through the tracker (*backsplash*) and traverse the ACD, erroneously triggering a veto and leading to the rejection of valid  $\gamma$ -ray events. To mitigate the *backsplash* effect and prevent self-veto in the LAT, the ACD is segmented. This segmentation, along with information from the tracker, allows to determine if the detected photon originated from lower detector layers as a secondary product. In such cases, the event is not automatically rejected as a cosmic ray.

### 3.3 Event Classification

At high energies, events are classified based on the probability that they correspond to a true photon detection. Fermi divides these events into four main classes: *Transient*, *Source*, *Source Veto*, and *UltraClean Veto*, ordered from the most inclusive to the most restrictive. The *Transient* class collects the largest number of events, while the *UltraClean Veto* class applies the most stringent selection criteria and thus collects the fewest.

In addition to this classification, there exists another one based on the topology of the event. This includes three classes: *Front*, *Back*, and *Total*. Unlike the previous categorization, these are not based on the probability of being a photon, but rather on where the conversion vertex of the pair-production event occurs within the tracker. Indeed, in the lower part of each tower, the tungsten layers are thicker than those in the upper part and they can detect events that have escaped the thinner upper layers, such as high-energy photon. The *Front* class refers to events in which the vertex lies in the upper, thinner section of the tracker, whereas the *Back* class includes those whose vertex occurs in the lower, thicker section. The *Total* class comprises all events, regardless of their conversion location.

## 4 Data analysis

The  $\gamma$ -ray emission from PSR J2229+6114 was analyzed. The data corresponding to this pulsar were downloaded directly from the LAT data server by entering the objectmm coordinates, reported in Tab. 2, and converting them to degrees (RA = 337.272°, DEC = 61.2359°). A time interval of 90 days was selected, from 2008-10-05

to 2009-01-03 (see Tab. 2). We searched for events with energies between 100 and 500,000 MeV within a search radius of 4°, slightly larger than the LAT point spread function (PSF) at 100 MeV. The query returned two files: a event file (FT1) containing the photon data, and a spacecraft file (FT2) containing the spacecraft data. The FT1 file also includes the Good Time Intervals (GTIs), which are the time periods during which the data acquisition is considered valid for scientific analysis and corresponds to the times when the LAT was collecting data. Indeed, the LAT does not collect data while the observatory is transiting the Southern Atlantic Anomaly (SAA, a region in Earth's magnetic field where the field is significantly weaker than usual, allowing charged particles to dip closer to the planet's surface), or during rare events such as software updates or spacecraft maneuvers. In addition, the observed object will most likely not be in the field of view during the entire time that the LAT is taking data.

**Table 2:** Parameters of PSR J2229+6114 known from the literature.

PSR J2229+6114	
Right Ascension (RA) [hh:mm:ss]	22:29:05.280000
Declination (DEC) [dd:mm:ss]	61:14:09.300000
$f_0$ [Hz]	19.3639
$f_1$ [Hz/s]	$-2.92006 \times 10^{-11}$
Time Range [MJD]	54744–54834
Time Range [MET]	244857601– 252633602
Time Range [Gregorian]	2008-10-05 00:00:00– 2009-01-03 00:00:00

Before proceeding with data analysis, several preliminary operations were necessary. First, the time interval during which the detected photons could be considered valid was determined, that is, the interval for which the corresponding spacecraft data were available at the moment of detection. The photon arrival times contained in the FT1 file were examined, and only those detected between 1000 seconds after the beginning and 1000 seconds before the end of the spacecraft data range (FT2 file) were selected. The resulting valid time interval is 244858573.6 to 252632660.6 seconds, expressed in MET (Mission Elapsed Time). Next, using the Fermi tool `gt-select`<sup>2</sup>, the data were filtered by selecting photons within the valid time range, with energies above 100 MeV and located within a radius of 3° (i.e., approximately the LAT PSF at 100 MeV) around the selected coordinates. We also chose the source photon class (evclass=128) and both front and back types (evtype=3). Additionally, only photons for which the LAT was pointing at a maximum zenith angle of 100° were retained, in order to reduce contamination from Earth's albedo (a cutoff of 90° was not chosen to allow the inclusion of more photons).

Subsequently, the `gtmktime` tool<sup>3</sup> was used to exclude all photons outside the valid Good Time Intervals (GTIs).

<sup>2</sup>`gtselect` creates a filtered FITS file by selecting rows from an input event data file based on user-specified cuts that are applied to each row of the input file [7].

<sup>3</sup>`gtmktime` updates the GTI extension of the FT1 file by applying cuts based on spacecraft parameters contained in the FT2 file (pointing and livetime history), as well as on the existing GTIs in the event data file. All events outside this new set of GTIs are removed from the file [7].

This step is essential for computing correct exposure. Following the recommendations provided in [7], the following cuts were applied:

- (DATA\\_QUAL==1) && (LAT\\_CONFIG==1) && ABS(ROCK\\_ANGLE)<52, which selected good data runs and avoided pointing, that is when the LAT is not operating in sky-survey mode;
- ROI-based zenith angle cut [ ] yes, to exclude time intervals during which the buffer zone defined by the zenith angle cut intersects the Region of Interest (ROI). This option is particularly important when working with small ROIs (less than 20°), as the target source may approach the Earth's limb, which can result in significant contamination from atmospheric gamma rays.

#### 4.1 Photon barycentering

The measured photon arrival times are affected by the relative motion of GLAST within the Solar System, as well as by relativistic effects. In order to analyze the signal periodicity, it was therefore necessary to apply barycentric corrections to compensate for these effects:

$$T = t + \delta t = t + \Delta_{\text{Roemer}} + \Delta_{\text{Shapiro}} + \Delta_{\text{Einstein}} + \Delta_{\text{Binary}} \quad (9)$$

where  $\Delta_{\text{Roemer}}$  is the Roemer delay, accounting for the time taken by the photon to travel from the satellite to the Solar System barycenter;  $\Delta_{\text{Shapiro}}$  is the relativistic delay due to the curvature of spacetime caused by the gravitational field of the Sun;  $\Delta_{\text{Einstein}}$  is a corrective term that accounts for time dilation and adjusts the difference between the proper time of the satellite and the barycentric time; and  $\Delta_{\text{Binary}}$  is a correction applied only if the source is part of a binary system, accounting for variations in the arrival time due to the orbital motion of the source around the system's barycenter. These corrections convert the photon arrival times (originally expressed in Terrestrial Time, TT, at the spacecraft) into the corresponding times at the Solar System Barycenter (SSB).

The barycentric correction was performed using the `gtbary` tool [6], which applies barycentering time correction to an event file using spacecraft orbit files.

#### 4.2 Periodicity Search

After correcting the photon arrival times to the Solar System barycenter, we proceeded to search for periodicities in the signal. This was done using the  $Z_n^2$  statistic, as previously discussed in Sec. 2.4.

To begin with, we calculated the pulse phases according to Eq. 7. We chose the central time of the observation as the timing epoch, resulting in  $t_0 = 248694235.38002062$  s (expressed in MET). We then assumed the values  $f_0 = f_0^{\text{central}}$  and  $f_1 = f_1^{\text{central}}$  reported in Tab. 2 as the central values of the frequency and its time derivative at epoch  $t_0$ . Finally, we converted all photon arrival times into their corresponding phases. Any negative phases were transformed to the  $[0, 1]$  interval by adding 1.

Next, we scanned the frequency space around the central values  $f_0^{\text{central}}$  and  $f_1^{\text{central}}$  in fractions of the Fourier resolution  $f_F = 1/T$ , which represents the spacing between two independent frequencies in a Fourier Transform, where  $T$  is the duration of the observation ( $7.66 \cdot 10^6$

s). We chose resolutions of  $df_0 = 1/T = (1.30 \times 10^{-7})$  Hz for the frequency and  $df_1 = 0.01/T^2 = (1.70 \times 10^{-16})$  Hz/s for its derivative. We then created a  $1000 \times 30$  grid centered on our central values, with the frequencies  $f_0$  along the x-axis and the derivatives  $f_1$  along the y-axis, using steps of  $df_0$  and  $df_1$ . We proceeded to determine the best values of  $f_0$  and  $f_1$  by searching for those that maximize the  $Z_n^2$  statistic. We applied Eq. 8 to the phases calculated for all possible combinations of values in the grid. We used  $n = 4$  harmonics and  $N = 11154$  is the number of photons and performed 1000 trials on  $f_0$  and 60 on  $f_1$ . We then plotted the results in a figure with frequency on the x-axis, frequency derivative on the y-axis, and  $Z_n^2$  values represented by the colorbar. The results are shown in Fig. 6. Finally, we identified the pair  $(f_0, f_1)$  that maximizes the  $Z_n^2$  statistic, representing the best rotational parameters of the pulsar. We obtained a frequency of  $f_0 = 19.36391685 \pm 0.00000013$  Hz and a frequency derivative of  $f_1 = -(2.919549 \pm 0.000017) \times 10^{-12}$  Hz/s. The uncertainties were taken to be equal to the resolutions  $df_0$  and  $df_1$ .

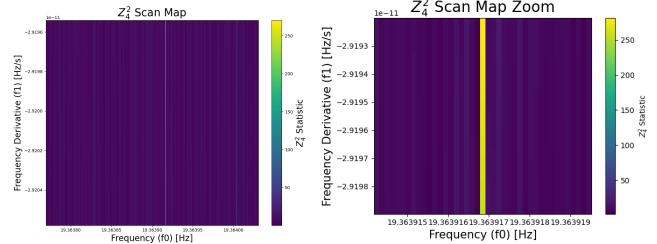


**Figure 6:** Map of  $Z_4^2$  values computed over the frequency space around the central values  $f_0 = f_0^{\text{central}}$  and  $f_1 = f_1^{\text{central}}$ . The x-axis shows the frequencies  $f_0$ , while the y-axis shows the frequency derivatives  $f_1$ . The color bar indicates the corresponding  $Z_4^2$  values. A well-defined vertical yellow stripe can be observed, corresponding to the values that maximize the statistic. The panel on the left shows a zoomed-in view of this region.

To further demonstrate that the pair  $(f_0, f_1)$  we found is correct, we plotted a scatter plot of time versus phase. Each point represents a photon, so if the parameters are accurate we should observe vertically aligned clusters of photons corresponding to the pulsation peaks. These clusters indicate that there is no phase drift over time due to an incorrect choice of  $(f_0, f_1)$ . The graph is shown in Fig. 7. We can see faint clusters just before the pulse  $\phi = 0.4$ .

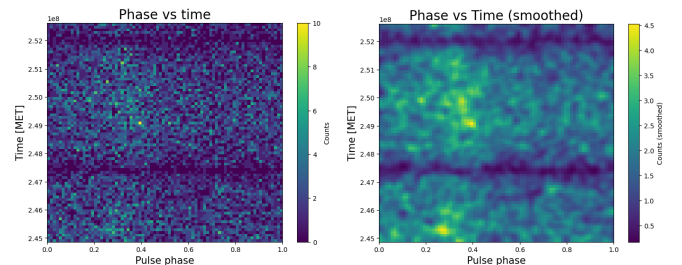


**Figure 7:** Scatter plot of time versus phase. In the left panel, a vertical cluster of photons can be glimpsed on the left side of the map. To enhance its visibility, the right panel shows the same data after applying a Gaussian filter to reduce noise. The Gaussian filter is a smoothing technique that reduces noise in the data while preserving the signal structure; it works by applying a weighted average based on a Gaussian (bell-shaped) function. A vertical cluster of photons is clearly visible. We also notice some dark horizontal lines in both panels, probably due to periods when LAT did not acquire valid photons.

### 4.3 Phaseogram Characterization

Starting from the  $(f_0, f_1)$  values obtained with the  $Z_n^2$  statistical test, we proceeded to study the pulsation profile by building phaseograms in different energy ranges. The phases were computed according to Eq. 7 over the time interval  $T$ , using the central time of the observation as the timing epoch  $t_0$ . Any negative phases were transformed into the  $[0, 1]$  interval by adding 1, as discussed in Sec. 4.2. To better visualize the main peak (which would otherwise cross phase zero) we applied a fixed phase offset  $\phi(t_0) = 0.1$  in Eq. 7. We then produced histograms using 50 bins per rotation period (as used in [1]). We assumed Poisson noise and assigned to each bin count an error equal to the square root of the number of counts in that bin,  $\sqrt{N_{\text{counts-bin}}}$ .

In Fig. 8, the phaseogram for photons with energies above 100 MeV is shown. As we can see in the first panel, there is a strong contribution from background emission (approximately 150 counts per bin). However, a single broad and asymmetric peak remains visible. To improve its visibility, we reproduced the plot starting from a baseline level of 150 counts (second panel). The pulsation signal is now more clearly visible.

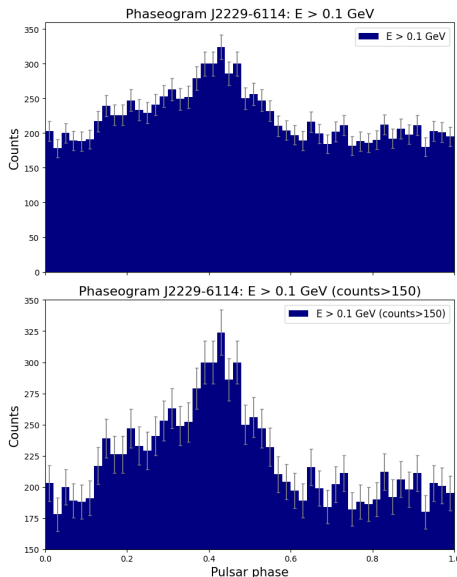


**Figure 8:** Phaseogram for photons with energies above 100 MeV. In the bottom panel, a baseline of 150 counts was set to enhance the visibility of the peak. A single broad and asymmetric peak is clearly visible. A fixed phase offset  $\phi(t_0) = 0.1$  was applied to prevent the peak from crossing the zero phase.

We then produced the phaseograms for the following energy ranges:  $E > 0.1 \text{ GeV}$ ,  $0.1 \text{ GeV} < E < 0.3 \text{ GeV}$ ,  $0.3 \text{ GeV} < E < 1 \text{ GeV}$ ,  $1 \text{ GeV} < E < 3 \text{ GeV}$ , and  $E > 3 \text{ GeV}$ . The corresponding histograms are shown in Fig. 9a. To better visualize the peaks, different baseline levels were chosen for each energy range. The corresponding photon maps for the different energy intervals are also shown in Fig. 9b. We also calculated the phase associated with each peak from the phaseograms. The uncertainty for each peak was assigned as the width of the binning interval, i.e.,  $1/50$ . The results are listed in Tab. 3.

### 4.4 Physical Characterization of J2229+6114

Starting from the frequency  $f_0$  and its derivative  $f_1$  obtained from the  $Z_n^2$  test in Sec. 4.2, we finally calculated

**Table 3:** Peak phases and associated errors for different energy bands.

Energy range	Peak phase	Error
$E > 0.1 \text{ GeV}$	0.43	$\pm 0.02$
$E > 3 \text{ GeV}$	0.35	$\pm 0.02$
$1 < E < 3 \text{ GeV}$	0.43	$\pm 0.02$
$0.3 < E < 1 \text{ GeV}$	0.47	$\pm 0.02$
$0.1 < E < 0.3 \text{ GeV}$	0.41	$\pm 0.02$

the following main physical quantities characterizing the pulsar J2229+6114:

1. the pulsar period  $P$ , calculated as the inverse of the frequency  $1/f_0$ ;
2. the time derivative of the period  $\dot{P} = -f_1/f_0^2$ ;
3. the magnitude of the magnetic field  $B$ , calculated using Eq. 5;
4. the characteristic age  $\tau_c$ , through Eq. 6;
5. the rotational energy loss rate  $\dot{E}_{\text{rot}}$ , also called spin-down luminosity, using Eq. 3.

The errors associated with the calculated quantities were obtained via standard error propagation:

$$\sigma_f = \sqrt{\sum_{i=1}^n \left( \frac{\partial f}{\partial x_i} \right)^2 \sigma_{x_i}^2}. \quad (10)$$

The results are reported in Tab. 4, where they are compared with those available in the literature ([1] and [9]).

### 4.5 J2229+6114 in the $P-\dot{P}$ diagram

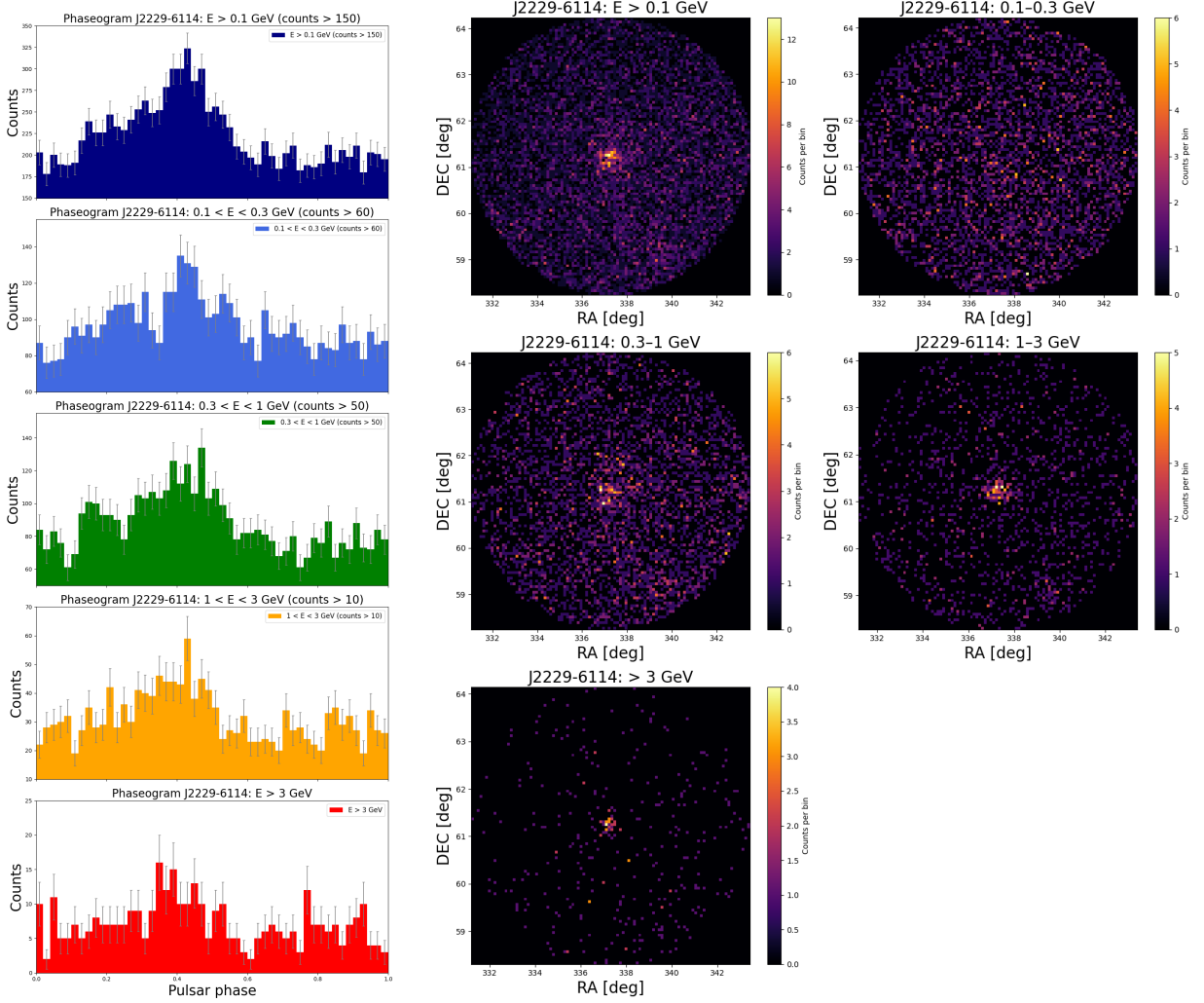
Based on the results obtained in Sec. 4.4, we placed PSR J2229+6114 on the  $P-\dot{P}$  diagram (see Sec. 2.3), together with the known pulsars from the ATNF Pulsar Catalogue [2]. The results are shown in Fig. 10. In agreement with the discussion in Sec. 2.3, being a young pulsar, J2229+6114 is correctly located in the upper left region of the diagram.

## 5 Discussion

### 5.1 High Background Level

The data analysis revealed a high background level, which made the visualization of the signal more difficult. Despite this, the  $Z_n^2$  test successfully converged and identified consistent best values for  $f_0$  and  $f_1$ , demonstrating its ability to detect physical signals even in the presence of significant noise (as discussed in Sec. 2.4).

In Sec. 4.2, we plotted the time vs. phase scatter plot (see Fig. 7) to verify the correctness of the best-fit values  $f_0$  and  $f_1$  obtained from the  $Z_n^2$  statistic. However, the expected vertical photon clusters were difficult to visualize and required smoothing with a Gaussian filter to enhance their visibility. This does not imply that the derived values are incorrect, as they remain consistent with subsequent analyses. The lack of clearly visible clusters in Fig. 7 can be attributed to the very high background level, from which the physical signal emerges only slightly, making it hard to identify qualitatively.



(a) Phaseograms for photons in different energy ranges.

(b) Map of the photons in the different considered energy ranges. The x-axis shows the right ascension, while the y-axis shows the declination, both in degrees.

**Figure 9:** Comparison between (a) the phaseograms for the pulsar and (b) the spatial map of the photons in different energy ranges. In the phaseograms in Fig. 9a, a single broad and asymmetric peak is clearly visible in all the phaseograms. A fixed phase offset  $\phi(t_0) = 0.1$  was applied to prevent the peak from crossing the zero phase. The baseline level is reported in the labels of each panel. In the photon maps in Fig. 9b, a binning of  $\text{deg}/\text{pix} \sim 0.1$  was chosen [8].

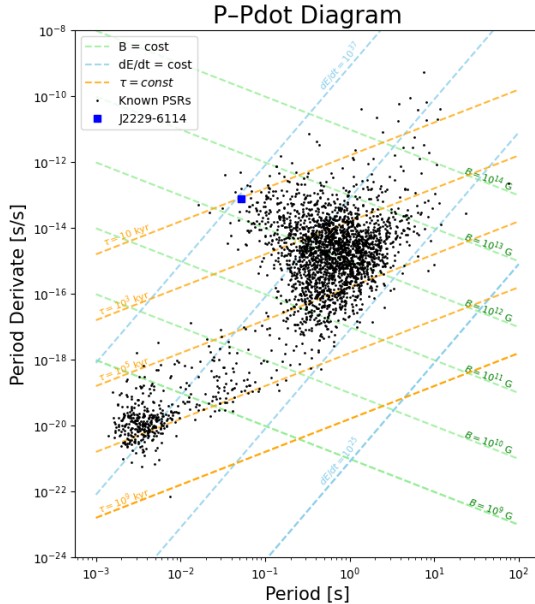


**Figure 10:**  $P-\dot{P}$  diagram. The pulsars from the ATNF Pulsar Catalogue [2] are shown as black dots. The typical structure of the diagram is visible, with a higher concentration of pulsars in the central region and the millisecond pulsar population in the bottom left. PSR J2229+6114 is marked with a blue square and is correctly located in the region corresponding to newly formed pulsars. The dashed lines represent isolines of magnetic field strength  $B$  (green), characteristic age  $\tau_c$  (orange), and spin-down luminosity  $\dot{E}_{\text{rot}}$  (light blue).

**Table 4:** Pulsar parameters with calculated values, associated uncertainties, and space for comparison with values from the literature (see [1] and [9]). The values from [9] are marked with an asterisk (\*) and refer to an earlier epoch (2001) compared to the data analyzed in this work. The values from [1] correspond to the same epoch as our observations.

Quantity	Literature value	Calculated value	Uncertainty
Period (ms)	51.6	51.6424444386	0.0000000004
Period derivative (s/s)	$7.83 \times 10^{-14} *$	$7.7863 \times 10^{-14}$	$0.0000001 \times 10^{-14}$
Magnetic field (G)	$2.0 \times 10^{12} *$	$2.02916828 \times 10^{12}$	$0.00000002 \times 10^{12}$
Characteristic age (years)	10460	10515.7634	0.0002
Spin-down power (erg/s)	$2.2 \times 10^{37}$	$2.23186924 \times 10^{37}$	$0.00000003 \times 10^{37}$

## 5.2 Phaseograms analysis

By examining the phaseograms shown in Fig. 9a, we can analyze the structure of the signal at different energies. The first panel includes all events with energies above 100 MeV. The signal peak appears well-defined and distinct from the noise, though there is a strong background contribution.

Analyzing the different energy ranges, we observe that the number of counts in the phaseograms remains roughly constant at low energies ( $E < 1\text{GeV}$ ), but decreases in the intermediate range ( $1\text{GeV} < E < 3\text{GeV}$ ), and then drops drastically above 3 GeV. We therefore conclude that most of the emission is concentrated below 3 GeV, consistent with the spectral energy distribution reported in [1]. We also note that the background contribution is significant up to 1 GeV, but then declines sharply at higher energies.

The peak profile remains well defined up to 3 GeV, but becomes almost indistinguishable from noise at higher energies. From the data in Tab. 3, we see that the peak in the 300 MeV–1 GeV range is slightly shifted toward higher phases compared to the other energy bands (with the exception of the  $> 3\text{ GeV}$  case). The peak profile is broad and asymmetric, in agreement with the results obtained by A.A.Abdo et al.[1] (see Fig. 11).

In Fig. 9b, we show the photon maps for the different energy ranges. At low energies, the background contribution dominates, making the signal indistinguishable in the maps. However, in the phaseograms, the signal remains clearly visible, further demonstrating the ability of the  $Z_n^2$  statistic to reveal physical signals even in the presence of strong noise.

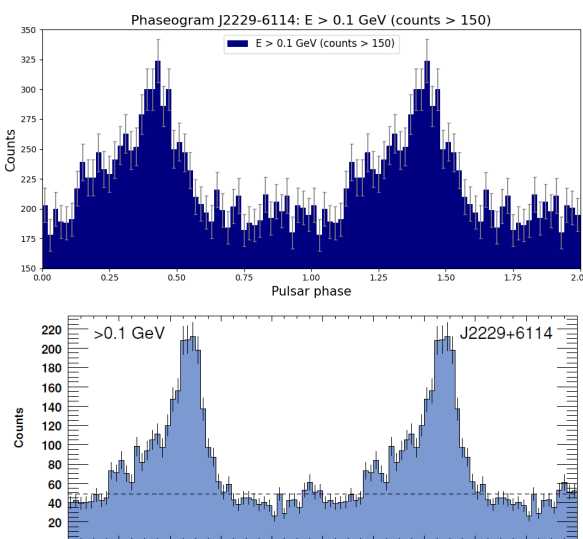


**Figure 11:** Comparison between the peak profile obtained in this work (top) and that of Abdo et al. (bottom) [1]. The two profiles show good agreement. The phaseogram was plotted over two rotation periods with 50 bins per period.

## 5.3 Physical quantities of J2229+6114

The physical parameters characterizing PSR J2229–6114 derived from our data analysis are reported in Tab. 4. The results are compared with those obtained by A. A. Abdo et al.[1] based on LAT data collected over the same period used in our analysis (2008–2009). The values of  $\dot{P}$  and  $B$ , which were not reported in that paper, were instead taken from J. P. Halpern et al.[9], who derived them from observations in 2001. We can see that our results are consistent with the expected values. However, our error estimates, based on the resolution with which we scanned the frequency space (see Sec.4.2) and standard error propagation (see Sec.4.4), turn out to be underestimated. More reliable estimates could be obtained by applying statistical criteria or by analyzing systematic errors and the instrument response functions.

## 6 Conclusion

The objectives set for this experience were achieved, leading to a successful analysis of the periodic gamma-ray emission from J2229+6114. The data provided by LAT were correctly selected and barycentered. They were then analyzed to search for evidence of periodic signals by applying the  $Z_n^2$  statistic, resulting in best-fit values of  $f_0 = 19.36391685 \pm 0.00000013$  Hz and a time derivative of  $f_1 = (-2.91921 \pm 0.00002) \times 10^{-12}$  Hz/s. Phaseograms were then constructed, and the periodic pulse profile was studied over different energy ranges. Finally, the main physical quantities characterizing J2229+6114 were derived (see Tab. 4). The results obtained are in good agreement with the values reported in the literature.

During the analysis, two main issues were encountered: the presence of a very strong background and the lack of an accurate estimation of the uncertainties associated with the measured physical quantities. Improved analysis using detailed models for the background and diffuse emission, as well as more accurate uncertainty estimates derived from statistical methods or a careful study of the instrumental response, are necessary.

## References

- [1] A. A. Abdo et al. “FERMI LARGE AREA TELESCOPE DETECTION OF PULSED  $\gamma$ -RAYS FROM THE VELA-LIKE PULSARS PSR J1048-5832 AND PSR J2229+6114”. In: *The Astrophysical Journal* (Nov. 2009). DOI: [10.1088/0004-637X/706/2/1331](https://doi.org/10.1088/0004-637X/706/2/1331). URL: <https://dx.doi.org/10.1088/0004-637X/706/2/1331>.
- [2] ATNF pulsar catalogue. URL: <https://www.atnf.csiro.au/research/pulsars/psrcat/>.

- [3] Matteo Bachetti et al. “Extending the  $Z_n^2$  and H Statistics to Generic Pulsed Profiles”. In: *The Astrophysical Journal* 909.1 (2021), p. 33. DOI: [10.3847/1538-4357/abda4a](https://doi.org/10.3847/1538-4357/abda4a). URL: <https://doi.org/10.3847/1538-4357/abda4a>.
- [4] R. Buccheri et al. “Search for pulsed  $\gamma$ -ray emission from radio pulsars in the COS-B data.” In: *Astronomy & Astrophysics* 128 (Dec. 1983), pp. 245–251. URL: <https://ui.adsabs.harvard.edu/abs/1983A%26A...128..245B/exportcitation>.
- [5] *Fermi LAT Performance*. URL: [https://www.slac.stanford.edu/exp/glast/groups/canda/lat\\_Perfor%5C-mance.htm](https://www.slac.stanford.edu/exp/glast/groups/canda/lat_Perfor%5C-mance.htm).
- [6] *Fermi Tools: Arrival Time Correction (gtbary) Tutorial*. URL: [https://fermi.gsfc.nasa.gov/ssc/data/analysis/scitools/arrival\\_time\\_tutorial.html](https://fermi.gsfc.nasa.gov/ssc/data/analysis/scitools/arrival_time_tutorial.html).
- [7] *Fermi Tools: Data Preparation*. URL: [https://fermi.gsfc.nasa.gov/ssc/data/analysis/scitools/data\\_preparation.html](https://fermi.gsfc.nasa.gov/ssc/data/analysis/scitools/data_preparation.html).
- [8] *Fermi: Pulsar Gating Tutorial*. URL: [https://fermi.gsfc.nasa.gov/ssc/data/analysis/scitools/pulsar\\_gating\\_tutorial.html](https://fermi.gsfc.nasa.gov/ssc/data/analysis/scitools/pulsar_gating_tutorial.html).
- [9] J. P. Halpern et al. “PSR J2229+6114: Discovery of an Energetic Young Pulsar in the Error Box of the EGRET Source 3EG J2227+6122”. In: *The Astrophysical Journal* 552.2 (Apr. 2001), pp. L125–L128. DOI: [10.1086/320347](https://doi.org/10.1086/320347).
- [10] G. Joncas and L. A. Higgs. In: *Astronomy and Astrophysics Supplement Series* 82 (1990), p. 113.
- [11] NASA. *Fermi Gamma-ray Telescope*. URL: <https://fermi.gsfc.nasa.gov/>.
- [12] Sergio Ortolani. *Dispense del corso di Astronomia, Università di Padova*.